DNS of swirling hydrogen-air premixed flames

Yuki Minamoto[1*], Kozo Aoki[2], Mamoru Tanahashi[2], Nedunchezhian Swaminathan[1]

[1] *Department of Engineering, University of Cambridge, Cambridge CB2 1PZ, United Kingdom*

[2] *Department of Mechanical and Aerospace Engineering, Tokyo Institute of Technology, 2-12-1 Ookayama, Meguro, Tokyo 152-8550, Japan*

∗Corresponding author
Email: ym270@cantab.net
Tel: +1 925 294 4556

Abstract

Direct numerical simulation is employed to investigate the turbulent flow characteristics and their effect on local flames for mean reaction rate modelling in turbulent swirling premixed flames. Two swirl numbers having significant effects on the formation of a central recirculation zone in the combustor are considered. The large velocity gradients in the higher swirl number case produce high turbulence intensity in a relatively upstream region compared to the lower swirl number case. The conditional Probability Density Functions (PDFs) of the reaction rate and dissipation rates of turbulent kinetic energy and scalar fluctuations are also examined. The PDFs show correlations between the turbulence energy dissipation and reaction rates and between the scalar dissipation and reaction rates, suggesting that the heat and radicals from the hot products trapped in the recirculation zones are mixed with the reactants, not only through scalar dissipation rate (i.e. scalar gradient) but also by small-scale processes of turbulence relevant to turbulent kinetic energy dissipation rate. Therefore, both scalar and velocity gradients have a strong influence on the chemical reactions through mixing of cold reactant and hot products. A conventional flamelet and EDC models are used to estimate the mean reaction rate, and to study the balance between these two mixing mechanisms. Although both models show a qualitative agreement with the DNS results, these models compensate their limitations each other, depending on the local turbulence and thermochemical conditions. A simple approach is proposed to exploit the advantages of these two models by considering the balance of two mixing mechanisms based on the chemical and turbulence time scales. The estimated mean reaction rate using the proposed model is significantly improved for the higher swirl number case, although the estimated value slightly shifts away from the DNS results for the lower swirl number case. The improved modelling estimate and the balance of turbulence and chemical time scales suggest that the locations of intense reaction zones are strongly related to the dissipation rates of both scalar and turbulent kinetic energy.

Keywords: Direct Numerical Simulation (DNS), Swirling flame, Eddy Dissipation Concept, Flamelet model

1. Introduction

There are strong demands for combustion devices to be more environmentally friendly. Especially, combustion engineers are facing urgent need to suppress pollutant emissions such as NO_x as well as to enhance combustion efficiency in gas turbine engines for power generation. One of many possible technologies to achieve these for the next generation combustion devices is lean-premixed combustion of either traditional fuels or renewable/alternative fuels. In premixed combustion, global flame characteristics can be controlled relatively straightforwardly to meet the environmental requirements, by changing the stoichiometry, dilution level and temperature of a reactant mixture. However, lean-premixed combustion is naturally unstable for a number of reasons, and this needs to be overcome.

Although many of these instabilities may be avoided by using MILD (Moderate and Intense Low-oxygen Dilution) premixed combustion, this technology has not yet fully matured for gas turbine combustion applications. There are several studies to investigate the relation between sound generation of flames and reaction rate dynamics in conventional premixed combustion [1, 2, 3, 4], and they show that the combustion instabilities are susceptible to the temperature and heat release rate fluctuations. Also, temperature fluctuations have significant influence on pollutant formation rate and emissions [5]. Thus, accurate and robust modelling of heat release rate is one of the keys to achieve "greener" combustion devices.

Among many possible burner types, swirl burners would be of particular interests for the advanced combustion devices such as gas turbine engines. The bluff body configuration would stabilise reaction zones through recirculation of burnt gases, and the swirl flow helps efficient mixing of reactants. The dynamics of swirl flames have been studied for premixed combustion and the literature is summarised in [6], indicating their potential for advanced combustion applications. However, unlike conventional turbulent planar, Bunsen, V-shaped and other zero- to two-dimensional canonical flames, the mean fluid velocity in a swirl burner involves strong three-dimensionality resulting from recirculation and vortex breakdown phenomena [7]. These flow features with strong shear create intense turbulence influencing the heat release rate. Therefore, understanding of the basic flow, turbulence generation and their effect on chemical reactions is imperative for modelling turbulent combustion in such flows.

Another difficulty to be faced for the next generation combustion devices is the fuel composition. The traditional fuels mainly consist of hydrocarbon while renewable and alternative fuels derived from biomass or gasification invariably contain hydrogen up to 90% by volume [8]. Although hydrogen helps to broaden the flammability limits of hydrocarbon fuels, it also triggers thermo-diffusive instability due to $Le \ll 1$, where Le is the Lewis number. Thus, a reasonable first step towards achieving modelling for turbulent combustion of next generation fuels would be to study non-unity Lewis number flames.

Experimental investigations of phase averaged combustion fields have furthered our understanding of heat release rate dynamics [9, 10]. However, the strong three-dimensionality of swirling flow makes experimental investigations challenging since two-dimensional measurements are used in general, although some three-dimensional estimates can be made using two-dimensional measurements [9, 11, 12]. Also, simulations of Reynolds averaged or filtered reacting fields are inadequate to study the interaction between turbulence and chemical reactions since these simulations require models for this interaction. Therefore, three-dimensional Direct Numerical Simulation (DNS) data of turbulent swirling flames of hydrogen-air mixture are analysed to investigate: (1) the effect of swirl on velocity and scalar fields, (2) turbulence characteristics and their effects on mixing of reactants, and (3) flame-turbulence interactions. Although DNS has several limitations such as simulation duration, computational domain size, etc., the use of this methodology is required to address the objectives of this study.

The details of DNS are explained in Sec. 2. The results are discussed in Sec. 3 starting with the general flow and flame features. This is followed by the results investigating the relation between reaction rate, turbulence and scalar gradients. The effect of turbulence and scalar dissipation on mean reaction rate is then discussed using conventional modelling approaches. The conclusions are summarised in the final section.

2. Direct Numerical Simulation

The turbulent swirling premixed flames are simulated by means of DNS approach employing fully compressible governing equations and a detailed kinetic mechanism for hydrogen-air combustion [13]. Although Moureau et al. [14] conducted a swirl flame DNS in a practical domain they employed laminar flamelet tabulated chemistry and thus the nature of turbulence–chemistry interaction is already presumed. In the present study, the hydrogen-air chemistry is fully resolved and all the scalars involved in the chemistry are transported in order to capture effects of turbulence on reaction zones in detail. Also, as discussed in Sec. 2.3, the turbulence conditions considered here are closer to those seen in practical devices [15] than the conditions reported in a previous DNS study of swirl flames [16]. Thus, the conditions and effects investigated in this study are complementary to these two previous studies.

2.1. Governing Equations

The governing equations are for conservation of mass, momentum, energy and mass fraction of species i. These equations are written as

mass:

$$\frac{\partial \rho}{\partial t}+\nabla\cdot(\rho\boldsymbol{u})=0, \tag{1}$$

momentum:

$$\frac{\partial(\rho\boldsymbol{u})}{\partial t}+\nabla\cdot(\rho\boldsymbol{u}\boldsymbol{u})=-\nabla\cdot\boldsymbol{P}, \tag{2}$$

energy:

$$\begin{aligned}\frac{\partial(\rho T)}{\partial t}+\nabla\cdot(\rho\boldsymbol{u}T)=&\frac{1}{\bar{c}_v}\nabla\cdot(\lambda_{th}\nabla T)-\frac{1}{\bar{c}_v}\sum_{i=1}^{N}(\rho Y_i\boldsymbol{V}_i c_{p,i}\cdot\nabla T)\\&-\frac{T}{\bar{c}_v}\sum_{i=1}^{N}\left[R_i\nabla\cdot(\rho Y_i\boldsymbol{V}_i)\right]-\frac{1}{\bar{c}_v}\boldsymbol{P}:(\nabla\boldsymbol{u})\\&-\frac{1}{\bar{c}_v}\sum_{i=1}^{N}(h_i\omega_i)+\frac{T}{\bar{c}_v}\sum_{i=1}^{N}(R_i\omega_i),\end{aligned} \tag{3}$$

mass fraction of i-th species:

$$\frac{\partial(\rho Y_i)}{\partial t}+\nabla\cdot(\rho\boldsymbol{u}Y_i)=-\nabla\cdot(\rho Y_i\boldsymbol{V_i})+\omega_i, \tag{4}$$

where λ_{th}, h_i, R_i and ω_i denote mixture thermal conductivity, specific enthalpy, characteristic gas constant and reaction rate of species i, respectively. The stress tensor $\boldsymbol{P}$ is:

$$\boldsymbol{P}=\left[p+\left(\frac{2}{3}\mu-\kappa\right)(\nabla\cdot\boldsymbol{u})\right]\boldsymbol{I}-\mu\left[(\nabla\boldsymbol{u})+(\nabla\boldsymbol{u})^T\right], \tag{5}$$

where μ is the dynamic viscosity and κ is the bulk viscosity of the mixture. The mixture averaged specific heat capacity at constant volume is given by

$$\bar{c}_v=\sum_{i=1}^{N}(c_{v,i}Y_i). \tag{6}$$

The diffusion velocity of species i, $\boldsymbol{V_i}$, is modelled using the Fickian type diffusion. Other symbols have their usual meanings.

The adiabatic combustion of a stoichiometric H_2-air mixture at 0.1 MPa is simulated using a detailed kinetic mechanism [17] consisting of 27 elementary reactions and 12 species (H_2, O_2, H_2O, O, H, OH, HO_2, H_2O_2, N_2, N, NO_2 and NO) including the effect of non-unity Lewis numbers. The temperature dependence of viscosity, thermal conductivity and diffusion coefficients are calculated using CHEMKIN-II packages [18, 19], which are modified for vector/parallel computations. The effects of Soret, Dufour, and pressure gradient are neglected.

These equations are discretised on a uniform mesh using a fourth order central difference scheme and are integrated in time using a third order Runge-Kutta scheme. Only the chemical source terms are handled using a point implicit method to reduce stiffness [20]. The same computer code has been used for a variety of turbulent combustion problems reported previously [21, 22, 23].

2.2. Configuration and Boundary Conditions

Figure 1 shows the numerical configuration and coordinate used in this study. The domain is a cuboid, having a size of $L_x \times L_y \times L_z$ in x, y and z directions. There is an inflow boundary at $x = 0$ and an outflow boundary at $x = L_x$. The boundaries in y and z directions are no-slip, iso-thermal wall with temperature fixed at T_u [24]. Note that the wall boundary layer is resolved and no numerical oscillation is observed under the numerical condition used in this study (explained in Sec. 2.3). These boundary conditions are based on the formulation of Navier-Stokes Characteristic Boundary Condition (NSCBC) [25, 26]. The shape of the inlet is a concentric annulus with an inner diameter of $D_{in} = 0.6$ mm and an outer diameter of $D_{out} = 2.5$ mm. By solving the steady Navier-Stokes equations in cylindrical coordinate with appropriate boundary conditions on the walls, mean profiles of radial u_r, azimuthal u_θ and axial u_x velocity components of an annular swirling flow at the inlet are obtained analytically as a function of radial distance, $r = \sqrt{y^2 + z^2}$ as

$$u_r = 0, \tag{7}$$

$$u_\theta = F_\theta \left(\frac{r^2}{3} + c_1 r + \frac{c_2}{r} \right) = F_\theta U_\theta, \tag{8}$$

$$u_x = u_x^b \left[\left(\frac{r}{R_{out}} \right)^2 + \frac{R^2 - 1}{\ln R} \ln \left(\frac{r}{R_{out}} \right) - 1 \right] c_3, \tag{9}$$

where $R_{out} = D_{out}/2$, $R_{in} = D_{in}/2$ and $R = R_{in}/R_{out}$. The bulk mean axial velocity u_x^b is to be set. The three integration constants, c_1, c_2 and c_3, are also determined by imposing no-slip wall conditions at $r = R_{in}$ and R_{out}, and the relation between u_x and u_x^b:

$$c_1 = -\frac{R_{out} \left(R^2 + R + 1 \right)}{3 \left(1 + R \right)}, \tag{10}$$

$$c_2 = \frac{R_{out}^3 R^2}{3 \left(1 + R \right)}, \tag{11}$$

$$c_3 = -\frac{2 \ln R}{R^2 \left(\ln R - 1 \right) + 1 + \ln R}. \tag{12}$$

The parameter F_θ is related to the external force for u_θ, which can be determined using the swirl number S defined as

$$S = \frac{\int_{R_{in}}^{R_{out}} u_\theta u_x r^2 dr}{\left(R_{out} - R_{in} \right) \int_{R_{in}}^{R_{out}} u_x^2 r dr}. \tag{13}$$

By substituting Eqs. (7)–(9) into Eq. (13),

$$F_\theta = S\frac{(R_{out} - R_{in}) \int_{R_{in}}^{R_{out}} u_x^2 r dr}{\int_{R_{in}}^{R_{out}} U_\theta u_x r^2 dr}. \tag{14}$$

The mean velocity obtained as above is used for a base flow at the inflow boundary. For the present DNS, velocity perturbations u_i' in direction i determined by a banded white noise are superimposed on the base flow following Wang et al. [27] as

$$u_i'(r, \theta, t) = \sum_{i=1}^{N_f} A\phi(r) \sin\left[2\pi f_j t + \Phi_{ij}(r, \theta, t)\right], \tag{15}$$

where $\phi(r)$ is the turbulence intensity variation given as

$$\phi(r) = 1 - \exp\left[-c_4\left(r - \frac{R_{out} + R_{in}}{2}\right)^2\right]. \tag{16}$$

The perturbation magnitude A at each frequency, $(f_j \mid j = 1, 2, \cdots N_f)$, is given as $A = u'_{max}/\sqrt{N_f}$, where u'_{max} is the maximum intensity of the velocity perturbation. The range of f_j includes the most unstable frequency, $f_u = 2/(R_{out} - R_{in})$, estimated from the mean velocity profile using the linear instability theory. Phase Φ_{ij} is given randomly by using random numbers. Each Φ_{ij} has its own randomly-determined lifetime after which Φ_{ij} is renewed for f_j. The number of modes N_f used in the present DNS is 120. The variation of turbulence intensity in Eq. (16) and the factor $c_4 \approx 9.2$ (mm^{-2}) are chosen to achieve a laminar-turbulence transition within the DNS domain for different S conditions. The obtained inflow velocity field is then mapped on the Cartesian coordinate at $x^+ = 0$ of the DNS domain.

2.3. Combustion and Numerical Conditions

In this study, adiabatic combustion of a stoichiometric hydrogen–air mixture at 0.1 MPa is simulated, and the reactant temperature is set to be $T_u = 700$ K. Under such a condition, the unstrained laminar flame speed S_L is 10.6 m/s, the thermal thickness, $\delta_{th} \equiv (T_b - T_u)/|\nabla T|_{\max}$, is 5.03×10^{-4} m, and the Zel'dovich thickness, $\delta_F \equiv \lambda_{th,u}/(\rho_u c_{p,u} S_L)$, is 1.8×10^{-5} m. The burnt mixture temperature is $T_b = 2340$ K. Two DNS cases, S06 and S12, with these thermochemical conditions are considered. For both cases, the bulk mean axial velocity at the inlet u_x^b is 200 m/s, and the maximum intensity of velocity perturbation u'_{max} is set to be 30 m/s which corresponds to the Root-Mean-Square (RMS) velocity fluctuation of 13.2 m/s at the inflow boundary. The swirl number is 0.6 for S06 and 1.2 for S12. These swirl number conditions produce the maximum azimuthal velocity of around u_x^b for S06 and $2u_x^b$ for S12 at the inflow boundary.

The size of DNS domain is set to be $L_x \times L_y \times L_z = 15 \times 10 \times 10\text{mm}^3$ for both cases, S06 and S12. This domain size is small compared to the practical and laboratory-scale combustors, and this may affect the present results regarding the basic flow characteristics. However, the use of DNS should provide detailed insights especially on the second and third objectives of this study noted in the introduction. The computational domain is discretised using $N_x \times N_y \times N_z = 769 \times 513 \times 513$ mesh points for both cases. These meshes ensure that there are at least 20 mesh points inside δ_{th}. Also, a cold flow DNS has been carried out with a mesh points of $385 \times 257 \times 257$ and $769 \times 513 \times 513$, and the difference of mesh points does not unduly change the cold flow results. The computational domain is initially filled with hot products which ignite the inflowing cold reactants to develop flames. The simulation was initially run for $11\tau_F$, where $\tau_F = \delta_{th}/S_L$, to ensure that the initial transients had left the computational domain. The simulation was then continued for about one additional τ_F and 7 data sets were collected for each case. These simulations have been run on Hitachi HA8000 cluster using 256 cores with a wall-clock time of about 3250 hours for each case.

3. Results and discussions

An instantaneous iso-surface of a reaction rate c_T is shown for S06 and S12 in Fig. 1. This iso-surface of c_T clearly shows the effect of swirl. Here, the reaction progress variable is defined using temperature T as

$$c_T = \frac{T - T_u}{T_b - T_u}. \tag{17}$$

The iso-surface is coloured using the instantaneous reaction rate, defined as

$$\omega_{c_T} = \frac{\dot{Q}}{c_p(T_b - T_u)}, \tag{18}$$

where $\dot{Q}$ is the heat release rate. The superscript "+" denotes an appropriate normalisation using the laminar flame quantities. For example, length, velocity, gradient of c_T and reaction rate are respectively normalised using δ_{th}, S_L, $1/\delta_{th}$ and $\rho_u S_L/\delta_{th}$. The two-dimensional cross-section denoted by red lines shows the location of 2D x-y plane considered in the following discussions. The iso-surface shows intense convolution for S12 compared to S06, showing a possibility that S12 involves higher turbulence intensity. The iso-surface of S06 has rippling shape, indicating the effect of Kelvin-Helmholtz (KH) instability. The KH instability is not visually observed for S12 due to the strong convolution of the iso-surface. This strong convolution suggests intense turbulence generation resulting from a vortex breakdown in the annular swirling jet for S12. The iso-surface shows that intense reactions occur relatively upstream locations for S12 compared to S06.

3.1. General flow features

The Reynolds average of a quantity Q is obtained by averaging Q over the sampling time and the four y-z quadrants using

$$\bar{Q}(x_0, y_0, z_0) = \frac{1}{4N_t} \sum_{n=1}^{N_t} \sum_{m=1}^{4} Q(x_m, y_m, z_m; n), \tag{19}$$

where

$$\begin{pmatrix} x_m \\ y_m \\ z_m \end{pmatrix} = \begin{pmatrix} 1 & 0 & 0 \\ 0 & \cos\theta_m & -\sin\theta_m \\ 0 & \sin\theta_m & \cos\theta_m \end{pmatrix} \begin{pmatrix} x_0 \\ y_0 \\ z_0 \end{pmatrix}, \tag{20}$$

and $\theta_m = \pi\,(m-1)\,/2$, $0 \le x_0 \le L_x$, $0 \le y_0 \le L_y/2$ and $0 \le z_0 \le L_z/2$. The number of data sets collected over the sampling period is denoted by N_t $(= 7)$. The density weighted average $\tilde{Q}$ is then computed as $\tilde{Q} = \overline{\rho Q}/\bar{\rho}$.

Figures 2 shows the variations of $\tilde{u}^+$ and $\tilde{v}^+$ for S06 and S12. These fields are shown in the x-y plane as explained in Fig. 1. The maximum $\tilde{u}^+$ is around $40S_L$ for both cases since the axial inlet velocity is the same for these two cases. However, while the high $\tilde{u}^+$ is convected simply downstream in S06, it spreads more in the radial direction in S12. It is worth to note that the radial velocity has been set to be zero at $x^+ = 0$; see that the large $\tilde{v}^+$ region is detached from $x^+ = 0$ in Figs. 2b and 2d. There is a small negative $\tilde{u}^+$ region inside the annular jet flow (left side of the high $\tilde{u}^+$ region in Fig. 2a marked as R1), suggesting the existence of a weak central recirculation zone near the inlet boundary in S06. In S12, however, the negative $\tilde{u}^+$ region is much larger as in Fig. 2c than that of S06, clearly showing that the central recirculation zone occupies a substantial portion of the domain. This larger recirculation zone is due to the centrifugal pressure gradient created by the strong swirling flow [28]. Given the intense recirculation zone, the maximum $\tilde{v}^+$ velocity is also larger by about four times of that in S06. The intense recirculating flow carries hot products back towards the upstream region (this point is discussed further in Sec. 3.2). These recirculated hot gases provide heat and radicals to the fresh reactants to sustain chemical reactions, and the dilatation due to the heat release accelerates the radial velocity further.

The behaviour of $\tilde{u}^+$ in S06 seems similar to that of a typical turbulent free shear flow since the radial velocity is not so intense. Figure 3 shows the mean axial velocity variation, $\tilde{u}/u_0$, with the radial distance, $y/y_{1/2}$ at several streamwise locations, x^+ =11.6, 15.5, 19.4, 23.3 and 27.2 for S06 and S12. Here, u_0 is the maximum of the mean axial velocity at each x^+ location. The half-distance $y_{1/2}$ is also defined as the radial distance at which $\tilde{u}(x, y_{1/2}, 0) = u_0/2$ is satisfied. This implies that $y_{1/2}$ is generally different for different x^+ locations. The variation of normalised velocity with the normalised y in Fig. 3a clearly shows self-similarity for S06, although $\tilde{u}/u_0$ inside the annular flow ($y/y_{1/2} < 0.5$) does not. This shows that the axial velocity in S06 is affected significantly by neither the weak inner recirculating flow nor the chemical reactions, and the annular flow behaves similar to typical free shear flows in most of the region. In contrast, the $\tilde{u}^+$ variation in S12 shown in Fig. 3b reveals a strong effect of recirculating flow and dilatation at all radial location except near the wall. Therefore, the swirl number in the present configuration has a significant effect on behaviour of the annular jet and on the formation of a central recirculation zone in the present configuration. Such an effect of the swirl induced vortex breakdown on the formation of a central recirculation zone has been also addressed in previous studies [29, 6, 30].

In the present DNS, a small velocity perturbations are added to aid laminar to turbulent flow transition as noted in Sec. 2.2. The small disturbance absorbs the energy from the base flows and eventually grows if the velocity gradients are strong enough. For both cases, the velocity gradient is relatively large as shown in Fig. 2. Figure 4 shows the variation of normalised turbulent kinetic energy, $\tilde{k}^+ = 0.5\widetilde{u_i'' u_i''}/S_L^2$, in the 2D x-y plane noted in Fig. 1. Here, a fluctuation Q'' of a quantity Q is calculated as $Q - \tilde{Q}$. The intense $\tilde{k}^+$ regions appear at different locations for S06 and S12 as shown in Fig. 4. The normalised turbulent kinetic energy generally increases with the x^+ distance in S06 while the turbulence simply decreases once it is generated in the upsteram region in S12. This is due to the difference of the base flow from which the energy is transferred to turbulent disturbances. The maximum value of $\tilde{k}^+$ also differs significantly despite that the initial disturbance at the inlet boundary has the same magnitude statistically and u_x^b is also the same. This clearly shows that the strong shear resulting from the larger radial and azimuthal velocity components in S12 encourages the small velocity disturbance to grow quickly to generate higher turbulence intensity in the upstream region.

The mean turbulence energy dissipation rate can be computed, including the dilatation effect, as

$$\tilde{\epsilon}_{turb} = \frac{2\overline{\nu\rho\,(S_{ij}S_{ij} - S_{ii}S_{ii}/3)}}{\bar{\rho}}. \tag{21}$$

Here, S_{ij} is the rate-of-strain tensor defined as $S_{ij} = 0.5(\partial u''_i/\partial x_j + \partial u''_j/\partial x_i)$. The turbulent length scale is obtained using $l_E = u'^3_{\mathrm{rms}}/\tilde{\epsilon}_{turb}$, where the RMS velocity is computed as $u'_{\mathrm{rms}} = (2\tilde{k}/3)^{1/2}$. Using l_E and u'_{rms}, the local turbulent combustion conditions in the present DNS cases can be examined using the regime diagram [31] and the diagram is shown in Fig. 5. The colour of each data point gradually changes with an increase of downstream distance, x^+ location, from green to purple for S06, and from blue to red for S12. As clearly observed in the figure, the Damköhler, $\mathrm{Da} \equiv (l_E/\delta_F)/(u'_{\mathrm{rms}}/S_L)$ (Karlovitz, $\mathrm{Ka} \equiv (u'_{\mathrm{rms}}/S_L)^{3/2}(l_E/\delta_F)^{-1/2}$) number generally decreases (increases) with the streamwise distance for S06 while it changes in the opposite direction for S12. Also, the maximum Reynolds number based on Taylor microscale Re_λ is around 100 for S06 and 210 for S12 (not shown), and they are observed in relatively downstream and upstream regions, respectively. The variation transition of the Reynolds number based on integral length scale $Re_{l_E} = u'_{\mathrm{rms}} l_E/\nu$ can be interpreted from Fig. 5.

The local turbulent combustion conditions range from “laminar flames” to “wrinkled flamelets” to “corrugated flamelets” to “thin reaction zones” regimes for both of the cases. A large number of local laminar flames are seen for the S06 case at an upstream location ($x^+ < 10$). Such laminar flames are not as frequently seen for S12 as S06 because of accelerated laminar–turbulence transition resulting from the vortex breakdown process in the annular jet noted in Fig. 3. Thus, based on the local turbulent combustion conditions, some of the local reaction zones in the upstream are expected to be thin, which may be treated as flamelets. This point is discussed further in Sec. 3.4.

3.2. Characteristics of scalar fields

Chemical reactions generate heat that can affect fluid flow in the combustor significantly through dilatation. Thus, the reaction progress variable based on temperature c_T and its reaction rate (normalised heat release rate) ω_{c_T} are studied. The influence of progress variable definition is discussed in the appendix. Figure 6 shows the instantaneous and Favre averaged c_T and $\omega_{c_T}^{+}$ for S06 and S12 on the same x-y plane marked in Fig. 1. For S06, the fresh reactants fed from the inflow boundary are convected as far as $x^+ \approx 12$ by the axial inlet velocity while the recirculation of the burnt gas does not seem to be intense. As a result, the high temperature region (i.e. $c_T > 0.95$) generally locates in the downstream, $x^+ > 24$, as seen in Figs. 6a and 6e. For S12, however, the hot products exist in both upstream and downstream regions, as seen in Figs. 6c and 6g. This shows that burnt gases are convected upstream by the strong recirculating flow in the region R1 observed in Fig. 2c. The recirculated hot gases provide neighbouring reactants with heat and radicals to sustain intense heat release.

The instantaneous reaction rate variations show consistent behaviour with the progress variable field. The high $\omega_{c_T}^{+}$ regions distribute along the streamwise direction from the inlet in S06 while the variation shows the effect of the recirculating flow in S12 as shown in Figs. 6b and 6d. For S12, the reaction zone locates in the region between inner (R1) and outer (R3) recirculation zones marked in Fig. 2c, and a similar behaviour has been reported in a study employing Large Eddy Simulation of a turbulent swirl flame with $S = 1.2$ [4].

The local instantaneous reaction zones seem to be thin with their thickness about δ_{th} over a substantial region, although some of them is distributed broadly, e.g. $(x^+, y^+) = (5, 3)$ in Fig. 6d, possibly due to the turbulence and reaction zone interactions. For both cases, the reaction zone thickness in the upstream region (e.g. $x^+ < 4$) just after the inlet seems thinner than δ_{th} due to strain thinning effect. Precessing vortex core (PVC) is another feature of combustion stabilised in swirling flows. Due to relatively small swirl number and possibly because of limited DNS domain size, clear PVC is not observed in S06 [28]. For S12, although neither Fig. 1b (3D) nor Fig. 6d (2D x-y plane) shows visible PVC despite the high swirl number, a 3D snapshot looking down in x-direction reveals the presence of the helix structure in ϵ_{turb} and ω_{c_T} fields (see Fig. 7). Clearly, the high reaction rate regions are "trapped" in part of the helix structure, suggesting an effect of PVC. However, as described in the next paragraph, this effect does not appear in the Reynolds averaged field because of the averaging in azimuthal direction.

The mean reaction rate $\bar{\omega}^+_{c_T}$ of S06 in Fig. 6f shows a clear flame brush closely following the high $\tilde{c}_T$ gradient observed in Fig. 6e. The thickness of the brush seems to be δ_{th}–$2\delta_{th}$, and the normalised maximum value is $\bar{\omega}^+_{c_T} \sim 0.7$, suggesting that the local flames may be similar to unstrained laminar flame in S06 in an average sense. For S12, there are two branches of thin flame brush due to the strong shear flows in $x^+ < 4$. However, the distinction between these branches become unclear for $x^+ > 4$. Also, most of the intense reaction zone seems to locate in the high $\tilde{k}^+$ region (compare with Figs. 6h and 4b) unlike S06, suggesting a possibility that there is a correlation of reaction rate and turbulence fields.

The instantaneous c_T in Figs. 6a and 6c suggests thin reaction zones near the burner exit, while the slope of c_T seems to vary significantly elsewhere, especially for S12. To clarify this behaviour, instantaneous scalar gradient, $|\nabla c_T|^+$, and its conditional average with c_T are shown and compared with the corresponding laminar flame in Figs. 8a and 8b. The conditional average shows a slight deviation from the laminar flame solution for S06 and a relatively large deviation for S12 at around $0.1 < c_T < 0.3$. The standard deviation is larger in S12 than S06 and maximum instantaneous value shows around 6.0 times and 8.0 times of the corresponding laminar flame value for S06 and S12. This result shows a possibility that the substantial amount of local turbulent flames does not present the characteristics similar to the laminar flame. The statistical behaviours of scalar gradient (scalar dissipation rate) and reaction rate are discussed in the next section.

3.3. Relation between reaction rate and dissipation rates

Comparing the turbulent kinetic energy and reaction rate fields shown respectively in Figs. 4 and 6, the mean reaction rate and turbulent RMS velocity seem to be directly correlated, especially for the S12 case. Figure 9 shows the variations of two mean reaction rate contours, $\bar{\omega}^+_{c_T} = 0.1$ and $\omega^+_{1/2}$, and Favre averaged turbulent kinetic energy dissipation rate $\tilde{\epsilon}^+_{turb}$ contours for S06 and S12. Here, $\omega_{1/2}$ is 50 % of the maximum $\bar{\omega}_{c_T}$ for each case. Note that only $\tilde{\epsilon}^+_{turb} \geq 100$ is shown. Both Figs. 9a and 9b show that the large reaction rate is likely to occur in regions where the turbulence dissipates its energy. This trend seems stronger in S12 than S06 and this can be explained based on an analogy between behaviours of scalar and turbulent kinetic energy dissipation rates as follows. Dissipation of turbulence energy into heat largely depends on the small-scale processes of turbulence. Such small-scale processes, where viscous effects are important, also play a role on mixing of cold reactants and hot products in premixed combustion and this mixing is a key phenomenon to sustain high reaction rate and thus heat release rates. While a substantial part of this mixing would be through large scalar gradients (i.e. scalar dissipation rate) in conventional premixed combustion, the small-scale viscous turbulence processes could also play an important role on this mixing in the present swirling flames given that the Ka is greater than unity locally as in Fig. 5.

The statistical relationship between the reaction rate and scalar dissipation rate may be studied using their joint PDF shown in Fig. 10. Here, the scalar dissipation rate is computed as $\epsilon_{c_T} = \alpha_c |\nabla c''_T|^2$, where α_c is the diffusivity of c_T (temperature). Note that the dissipation rates and probability densities are shown in logarithmic scales. The long ridge is well represented by the laminar flame solution in S06. This ridge, however, is shifted slightly towards higher values of the scalar dissipation rate in S12. This suggests an increased role of turbulence in the generation of ∇c_T in turbulent flames with large swirl number. Despite these insights, the high probability density at $\omega^+_{c_T} \sim 0$ obscures the behaviour of samples having large reaction rate which are of our interest. Therefore, conditional PDFs are investigated to gain further insights.

The conditional PDFs of scalar and turbulence dissipation rates and reaction rates are examined to study the statistical relationship between the turbulent kinetic energy dissipation rate ϵ_{turb}, scalar dissipation rate ϵ_{c_T} and reaction rate ω_{c_T} in Figs. 11 and 12. The conditional PDFs are computed using the Baye's theorem, and the samples are collected from the entire domain and sampling period. The number of sampling bins used is 150 (for Fig. 11) and 100 (for Fig. 12) for each sampling space to construct these conditional PDFs.

The PDF of turbulent kinetic energy dissipation rate conditioned on the reaction rate, $P(\ln \epsilon_{turb}^{+} | \omega_{c_T}^{+})$, is shown in Figs. 11a and 11b for S06 and S12. There is an approximate proportionality between the most probable $\ln\left(\epsilon_{turb}^{+}\right)$ and $\omega_{c_T}^{+}$ at $\omega_{c_T}^{+} < 0.1$ and this trend seems to be stronger for S12 compared to S06. For $\omega_{c_T}^{+} > 0.1$, the most probable $\ln\left(\epsilon_{turb}^{+}\right)$ shows an almost constant value of around 4.0 for S06 and 6.0 for S12, suggesting that the turbulence is very intense compared to the chemical scale (S_L/δ_{th}) used for the normalisation. The PDF of scalar dissipation rate conditioned on the reaction rate, $P(\ln \epsilon_{c_T}^{+} | \omega_{c_T}^{+})$, shown in Figs. 11c and 11d presents a well known behaviour showing that intense reaction zones are more likely to be in regions of high scalar dissipation rate. The most probable scalar dissipation rate at a given reaction rate closely follows the corresponding laminar flame solution for S06 while there is a deviation at $0 < \omega_{c_T}^{+} < 0.7$ for S12 as seen in Figs. 11c and 11d respectively. However, the proportional relation between scalar dissipation rate and reaction rate seems to hold reasonably well in a statistical sense.

Statistical behaviour of reaction rate at a given dissipation rate is also investigated using the PDF of $\omega_{c_T}^{+}$ conditioned on either $\ln\left(\epsilon_{turb}^{+}\right)$ or $\ln\left(\epsilon_{c_T}^{+}\right)$. Figures 12a and 12b show the PDF of $\omega_{c_T}^{+}$ conditioned on the turbulent kinetic energy dissipation rate, $P(\omega_{c_T}^{+} | \ln \epsilon_{turb}^{+})$ for S06 and S12, respectively. For S06, the peak PDF locates near $\omega_{c_T}^{+} \approx 0$ regardless of ϵ_{turb}^{+}. For S12,

Fig. 12b shows that the peak PDF location in $\omega_{c_T}^+$ space increases with an increase of ϵ_{turb}^+. Although the PDF distribution is not very sharp at larger ϵ_{turb}^+, the conditional PDF clearly shows that there is a consistent relation between the reaction rate and turbulent kinetic energy dissipation rate for S12. For both cases, the PDF has a long tail observed at each ϵ_{turb}^+ towards larger $\omega_{c_T}^+$, and the length of the tail increases with an increase of ϵ_{turb}^+.

The PDF of reaction rate conditioned on the scalar dissipation rate, $P(\omega_{c_T}^+|\ln\epsilon_{c_T}^+)$, is shown in Figs. 12c and 12d for S06 and S12. The most probable reaction rate generally increases with an increase in the scalar dissipation rate for both S06 and S12. The maximum $\ln(\epsilon_{c_T}^+)$ is greater than zero for both cases, meaning some of local flames have high scalar gradients compared to the laminar flame, which are possibly caused by stretching and straining effects of turbulence. Although such samples show a relatively high probability density, the reader should be careful that this is a PDF of $\omega_{c_T}^+$ conditioned on $\epsilon_{c_T}^+$ and the probability of having such high $\epsilon_{c_T}^+$ is relatively small (see Figs 11c and 11d). The unstrained laminar flame solution superimposed in Figs. 12c and 12d clarifies the turbulence effects. Although the overall trend is qualitatively similar between the laminar flame and turbulent flames, the probable $\omega_{c_T}^+$ shows much smaller values for turbulent flames at a given scalar dissipation rate, which is an artefact resulting from the behaviour of $\epsilon_{c_T}^+$ marginal PDF.

From a modelling view point, the two conditional PDFs, $P(\ln\epsilon_{turb}^+|\omega_{c_T}^+)$ and $P(\omega_{c_T}^+|\ln\epsilon_{turb}^+)$ shown respectively in Figs. 11 and 12, imply a relationship between turbulent kinetic energy dissipation rate and reaction rate. The relatively confined high probability density $P(\ln\epsilon_{turb}^+|\omega_{c_T}^+)$ in Fig. 11 and the long tail of $P(\omega^+_{c_T} | \ln \epsilon^+_{turb})$ in Fig. 12 confirm that having high turbulence energy dissipation rate is just a necessary condition and not a sufficient condition to have high $\omega^+_{c_T}$ in a statistical sense for swirling flames. As noted earlier, these PDFs are computed using the entire samples and these PDFs change negligibly when the samples collected within the flame brush, ie., $0.1 \leq \widetilde{c}_T \leq 0.9$, are used.

In relation to Figs. 11 and 12, cross-correlation coefficients C_c are computed for the instantaneous or mean reaction rate and turbulence or scalar dissipation rate fields. The correlation coefficient for two fields, $A(\boldsymbol{x}_i, t_j)$ and $B(\boldsymbol{x}_i, t_j)$, is computed as follows.

$$C_c = \frac{1}{n} \sum_{i,j} \frac{\left(A(\boldsymbol{x}_i, t_j) - \langle A \rangle\right) \left(B(\boldsymbol{x}_i, t_j) - \langle B \rangle\right)}{\sigma_A \sigma_B}, \tag{22}$$

where n is the total number of samples (e.g. $N_x \times N_y \times N_z \times$ number of snapshots in time), and σ_A and σ_B are the standard deviation of A and B respectively. The bracket $\langle \cdots \rangle$ is the volumetric average computed over the entire domain.

Table 1 shows the correlation coefficients for instantaneous and mean fields of S06 and S12. For the case S06 having lower turbulence level, the correlation of reaction rate with the scalar dissipation rate is improved compared to that with the turbulent kinetic energy dissipation rate. In contrast to this, the correlation of reaction rate to the viscous dissipation rate is large compared to the correlation with the scalar dissipation rate for the S12 case. Specifically, the correlation coefficient is about 0.9 for the mean fields as given in the table 1. This high correlation coefficient suggests that the mixing occurring at viscous scales are controlling the reaction rate in an averaged sense for the higher swirl number case. On the other hand, the small-scale mixing signified by the scalar gradient or molecular diffusion has a dominant influence on the reaction rate for the lower swirl number flame, S06. It is also to be recognised that the correlation coefficients for the instantaneous fields are smaller than for the mean fields. Generally small values seen in this table may be due to the use of samples from the entire computation domain and sampling period, as one may think. However, using the samples taken from the combusting regions, ie., $0.1 \leq c_T \leq 0.9$ or $0.1 \leq \widetilde{c}_T \leq 0.9$, does not change the values of these correlation coefficients unduly and these values are also given in table 1 within the brackets. The changes are not too big to change the conclusions as one observes in this table. Also, the averaging in time (over the number of time samples collected) is followed here because the time variation of these correlation coefficients for the instantaneous fields is observed to be small, the range of standard deviation is observed to be about 0.8% to 1.4% which are statistically small. The correlation coefficients discussed here support the insights obtained using the conditional PDFs in Figs. 11 and 12.

The conditional PDFs and the correlation coefficient support that the intense reaction rates occur in regions with relatively high scalar dissipation rate like in the conventional premixed combustion under $\mathrm{Da} > 1$, and they also occur in regions with high turbulent kinetic energy dissipation rate in turbulent premixed flames with large swirl number. Thus, the mixing of cold reactants with hot products trapped in neighbouring recirculation zones at scales relevant for combustion is supported by mixing facilitated by scales relevant for both scalar dissipation rate (molecular dissipation) and viscous dissipation rate (small-scale turbulent mixing).

3.4. Assessment using reaction rate closures

The previous discussion in Sec. 3.3 suggests a correlation between reaction rate and scalar dissipation rate, and reaction rate and turbulent kinetic energy dissipation rate. The relationship of the first two quantities, ω_{c_T} and ϵ_{c_T}, is extensively studied in past for premixed combustion without swirl.[32, 33, 34, 35, 36, 37, 38, 39]. Bray [32] proposed a reaction rate closure for premixed turbulent flames as:

$$\bar{\omega}_{c_T}^{B} = \frac{2\bar{\rho}}{2C_m - 1}\tilde{\epsilon}_{c_T}, \tag{23}$$

where C_m is a model parameter which usually takes around 0.7 [32]. This equation is exact in the limit of large Da, but also sufficiently valid for a range of turbulence conditions as reported in previous studies.[37, 40, 39] The physical mechanism suggested by this equation is that the mixing of cold reactants and hot products at scales relevant for combustion is dictated by the scalar dissipation rate to sustain reactions in an averaged sense. A phenomenological version of the above model based on the turbulent kinetic energy cascade concept was proposed by Spalding [41] and this model is commonly known as eddy-breakup model (EBU).

Based on the regime diagram shown in Fig. 5, the local turbulent combustion has hardly Da $\ll 1$ in the flames considered here. However, Ka > 1 in substantial regions and so the small scale turbulence is expected to dominate the mixing process to sustain chemical reactions locally. This mixing and its role on combustion is the basis for Eddy Dissipation Concept (EDC), originally proposed for non-premixed combustion [42] which was revised by

Ertesvag and Magnussen [43] to accommodate premixed combustion also. The EDC is similar to EBU in a sense that the turbulent energy cascade governing the turbulent time scale controls the mixing of reactants and products. However, while EBU assumes that small pockets of fresh gases breakdown to smaller burnt gas pockets following the Komogorov cascade of turbulence and the time scale associated to this breakdown process controls combustion, the EDC model employs a physical insight that the turbulence at "fine scales" (where viscous dissipation acts) influences the mixing thereby governs the state inside the fine structures. This denotes the rate of mixing of cold reactant and hot products for premixed combustion and it denotes the rate of mixing of fuel and oxidiser for non-premixed combustion [43]. Although this approach does not require to resolve the fine structures, the coupling of turbulent mixing and chemical reactions is effectively captured by computing the spatial extent of such fine structures in the domain as described below. The mean reaction rate is then described using the state of fine structures which is denoted by a superscript " * " below.

The fraction of the flow occupied by such fine structures is modelled as [43, 44]:

$$\gamma^* = 2.138 \left(\frac{\tilde{\nu} \tilde{\epsilon}_{turb}}{\tilde{k}^2} \right)^{1/4} . \tag{24}$$

Then, the state of the fine structures c_T^* is obtained by considering that these fine structure is a perfectly-stirred reactor (PSR) with a residence time τ_{res}, and initial states $\bar{\rho}$, $\tilde{T}$ and $\tilde{Y}_i$ in the present study. The PSR transport equation for c_T is:

$$\frac{dc_T}{dt} = -\frac{c_T - \tilde{c}_T}{\tau_{res}} + \frac{\omega_{c_T}^{\mathrm{PSR}}}{\rho}. \tag{25}$$

The steady solution obtained from Eq. (25) gives the state of fine structures,

c_T^*. Although the transport equation is written for progress variable here, similar equations for all species involved should be solved when Eq. (25) is directly integrated using a detailed chemical mechanism. In the EDC, the residence time τ_{res} corresponds to the average time scale during which the fluid resides inside the fine structures. This time scale is denoted by τ^* and computed as:

$$\tau^* = 0.408 \left(\frac{\tilde{\nu}}{\tilde{\epsilon}_{turb}} \right)^{1/2} . \tag{26}$$

The PSR reaction rate in the fine structures $\omega_{c_T}^{\mathrm{PSR}}$ can be computed using any chemical kinetics. In order to obtain the fine structure state c_T^*, Eq. (25) generally needs to be integrated in time using a small time step of Δt until the steady state is reached. Equation (25) may be calculated by taking $\Delta t \to \infty$ as [44]:

$$\frac{c_T^* - \tilde{c}_T}{\tau^*} = \frac{\omega_{c_T}^{\mathrm{PSR}}}{\rho}, \tag{27}$$

if the combustion condition is not close to extinction limit, since τ^* is generally small compared to τ_F under the present DNS conditions. Comparing c_T^* obtained by integrating Eq. (25) using small Δt and c_T^* calculated using Eq. (27), the maximum (average) difference in the final steady state value Δc_T^* is very small. These values are 0.048 (0.026) and 0.017 (0.015) for S06 and S12 respectively. Finally, the mean reaction rate is obtained using the fine structure state c_T^* as:[43, 44]

$$\bar{\omega}_{c_T}^E = \bar{\rho} \frac{{\gamma^*}^2}{\tau^*} \left(c_T^* - \tilde{c}_T \right). \tag{28}$$

Clearly, this model can include finite rate chemistry by considering the PSR reaction rate in the fine structure. If one combines Eqs. (27) and (28) then the mean reaction rate is directly related to the PSR reaction rate. In the limit of large Reynolds number, the small-scale turbulence can enter the reaction zone disturbing its structure. Under these conditions, the local reaction zone can be seen as a well-stirred reactor as suggested by the above equation. Also, since the mean production of c_T does not need to follow the Kolmogorov cascade exactly unlike EBU, the EDC can be applied for a range of turbulent combustion conditions. These two mean reaction rate closures are applied to the present swirl flames and the results are discussed next.

3.4.1. Estimation of mean reaction rate

The flamelet-based, Eq. 23, and the EDC approaches discussed in the previous sections are used here to contrast the role of scalar mixing and viscous dissipation processes in the present swirling flames. The modelled mean reaction rates, $\bar{\omega}_{c_T}^{B\ +}$ and $\bar{\omega}_{c_T}^{E\ +}$ respectively in Eqs. 23 and 28, are validated against the mean reaction rate $\bar{\omega}_{c_T}^{+}$ obtained directly from the DNS results. Note that $\widetilde{\epsilon}_{c_T}$, $\widetilde{k}$, $\widetilde{\epsilon}_{turb}$ and other quantities used in the models are obtained directly from the DNS data. Figure 13 shows the conditional PDFs of the modelled mean reaction rate, $P(\bar{\omega}_{c_T}^{B\ +}|\bar{\omega}_{c_T}^{+})$ and $P(\bar{\omega}_{c_T}^{E\ +}|\bar{\omega}_{c_T}^{+})$, for S06 and S12. The number of bins used for these PDFs is 30 in the $\bar{\omega}_{c_T}^{B\ +}$ and $\bar{\omega}_{c_T}^{E\ +}$ directions, and 30 (S06) and 20 (S12) in the $\bar{\omega}_{c_T}^{+}$ direction. The PDF is constructed from the modelled mean and DNS mean reaction rates fields in the x-y plane using the Bayes theorem as $P(\bar{\omega}_{c_T}^{B\ +}|\bar{\omega}_{c_T}^{+}) = P(\bar{\omega}_{c_T}^{B\ +}, \bar{\omega}_{c_T}^{+})/P(\bar{\omega}_{c_T}^{+})$ and $P(\bar{\omega}_{c_T}^{E\ +}|\bar{\omega}_{c_T}^{+}) = P(\bar{\omega}_{c_T}^{E\ +}, \bar{\omega}_{c_T}^{+})/P(\bar{\omega}_{c_T}^{+})$. The conditional averages, $\langle\bar{\omega}_{c_T}^{B\ +}|\bar{\omega}_{c_T}^{+}\rangle$ and $\langle\bar{\omega}_{c_T}^{E\ +}|\bar{\omega}_{c_T}^{+}\rangle$, are obtained by averaging in each $\bar{\omega}_{c_T}^{+}$ bin, and they are superimposed on the PDF.

The flamelet-based model using the scalar gradient alone underestimates the mean reaction rate for S06 and overestimates for S12 in most of $\bar{\omega}_{c_T}^{+}$

as seen in Figs. 13a and 13b. A drawback of Eq. (23) is that this model may not be able to include the effects of reaction zone interactions, since the mean reaction rate is modelled to be proportional to the mean scalar dissipation rate, and this proportionality cannot be guaranteed when there are flame interactions [45, 46]. Indeed, flame interactions are observed in these swirling flames as noted in Fig. 6d. Such interactions decrease the scalar dissipation rate while maintaining/increasing reaction rate [40]. In contrast, flame elements are stretched and strained by the local turbulence. Although the intensity of these effects varies, they lead to an increase of scalar gradient for higher turbulence conditions (compare Figs. 6a and 6c). In this case, Eq. (23) tends to overestimate the reaction rate. However, Eq. (23) reproduces qualitative trends, e.g. $0 < \bar{\omega}_{c_T}^{+} < 0.5$ for S06 and $0 < \bar{\omega}_{c_T}^{+} < 0.3$ for S12 as in Figs. 13a and 13b, suggesting that Eq. (23) models the combustion process in these flames adequately to some extent.

The mean reaction rate estimated using the EDC model involving the state of the viscously dissipative fine structure, Figs. 13c and 13d, shows a comparable performance to Eq. (23). Since the EDC assumes that the fine structures are like PSR, the local reacting elements with large scalar dissipation rates may not be adequately modelled by this approach as observed in Fig. 13d (e.g. $\bar{\omega}_{c_T}^{+} \approx 0.3$).

A close look at the conditional averages of ${\bar{\omega}_{c_T}^{B}}^{+}$ and ${\bar{\omega}_{c_T}^{E}}^{+}$ shows that the slope of $\langle {\bar{\omega}_{c_T}^{E}}^{+} | \bar{\omega}_{c_T}^{+} \rangle$ starts to increase when the slope of $\langle {\bar{\omega}_{c_T}^{B}}^{+} | \bar{\omega}_{c_T}^{+} \rangle$ starts to decrease, and vice versa (e.g. Figs. 13b and 13d at $\bar{\omega}_{c_T}^{+} \sim 0.3$). This suggests that these two models complement one another. These results show a possibility that the performance of these two models depends on the balance of two small-scale processes; one is turbulence processes resulting from velocity gradients or viscous processes and the other is the scalar dissipation rate coming from scalar gradients. For instance, flamelets are dominant and only Eq. (23) would work when the flame time scale is very short compared to the local turbulence time scale (large Da limit). In contrast, reaction zone interactions, intense stretching and straining of reaction zones occur when the turbulence time scale is relatively short. In this case, Eq. (23) does not hold and the EDC is likely to be more suitable locally.

The standard deviation of $\omega_{c_T}^{B\,+}$ and $\omega_{c_T}^{E\,+}$ shown for each $\omega_{c_T}^{+}$ in Fig. 13 also supports above reasoning. For the flamelet model in Eq. (23), the standard deviation is generally smaller in S06 than S12 as observed in Figs. 13a and 13b. This suggests that more flame elements can be modelled by Eq. (23) in S06 yielding a reduced standard deviation. For the EDC model, however, the deviation is larger in S06 than S12 as shown in Figs. 13c and 13d. This results from the relation between turbulence and chemical reactions discussed in Figs. 9, 11 and 12.

A possible way to exploit the advantages of both models is to combine these two modelled values according to a chemical and turbulence time scales as follows:

$$\bar{\omega}_{c_T}^{C} = \tau \cdot \bar{\omega}_{c_T}^{E} + (1-\tau) \cdot \bar{\omega}_{c_T}^{B}, \tag{29}$$

$$\tau = \frac{\tau_f}{\tau_t + \tau_f}, \tag{30}$$

where τ_f and τ_t are appropriate flame and turbulent time scales. Although there could be several possible ways to define these time scales, $\tau_f \equiv \delta_{th}/S_L$ and $\tau_t \equiv l_E/u'_{\mathrm{rms}}$ are used here as one choice. In the present turbulent combustion conditions, τ_f is about 2 to 10 times larger than τ_t in a substantial portion of the combusting region implying that the EDC based approach may be more appropriate. However, the local interplay between τ_f and τ_t can change leading to a preference for flamelet or EDC modelling approach locally. To include this change, the model in Eq. (29) is proposed in this study. The result of this model, $\bar{\omega}_{c_T}^{C+}$, is shown in Fig. 14 for S06 and S12. The conditional average, $\langle \omega_{c_T}^{C+} | \omega_{c_T}^{+} \rangle$, improves significantly as shown in Fig. 14b for the higher turbulence case S12, although this model is slightly worse than the stand-alone EDC model (Fig. 13c) for S06. The results in Fig. 14 suggest that Eq. (29) and the estimates of τ_t and τ_f for the flamelet and EDC models are reasonable.

4. Conclusions

Direct numerical simulation data sets are analysed to study turbulent flow characteristics, their effect on local flames, and their modelling in premixed turbulent swirl combustion. Two swirl numbers, $S = 0.6$ and 1.2, are considered. The azimuthal velocity has a significant effect on the generation of the central recirculation zone in the combustor. Although the radial velocity is set to be zero at the inlet boundary, it increases in the downstream locations due to vortex breakdown in the annular jet resulting from large azimuthal velocity and also due to dilatation resulting from combustion initiated by hot gases trapped in the central recirculation zone when the swirl number is large. These large radial and azimuthal velocity components produce higher velocity gradients, generating high turbulence intensity in a relatively upstream region for the higher swirl number case compared to $S = 0.6$ case.

Large reaction rates are observed in regions with large turbulent kinetic energy dissipation rate in an average sense, showing that the turbulent dissipation process influences chemical reactions. This suggests that the heat and radicals from the hot products trapped in the recirculation zones are mixed with the reactants locally not only by the scalar dissipation rate process but also by small-scale processes of turbulent dissipation occurring in those regions. The former is controlled by scalar gradients and the latter is controlled by velocity gradients. Thus, one must consider effects of both of these two gradients for modelling purposes. In order to understand these processes, conditional PDFs of reaction rate, scalar dissipation and turbulent kinetic energy dissipation rates are examined. The PDFs show a weak correlation between the turbulence dissipation rate and reaction rate for the lower swirl number case and this correlation becomes stronger for the higher swirl number case, although the conditional PDFs show that high turbulent kinetic energy dissipation rate is not a sufficient condition for high reaction rate. The PDFs of reaction rate conditioned on scalar dissipation rate show a comparable correlation between reaction rate and scalar dissipation rate for both cases. Therefore, both scalar and turbulence velocity gradients have strong influence on the chemical reactions through fine-scale mixing, and the balance between these two processes depends on the local turbulence and thermochemical conditions.

A conventional flamelet model involving scalar gradients as in Eq. (23), and EDC model involving the state of fine viscously dissipative structure as in Eq. (28), are used to estimate the mean reaction rate, and to assess the competition between the two mixing mechanisms for mixing cold reactants and hot products. Although both models show a reasonable qualitative agreement with the DNS results, they compensate each others' limitations when they are combined together appropriately.

A simple approach to unify these two models is proposed and tested here. The estimated mean reaction rate using this model, Eq. (29), is significantly improved for $S = 1.2$ case, although the estimated value slightly shifts away from the DNS results for $S = 0.6$ case. The improved result suggests that the competition between mixing mechanisms through the scalar and turbulence dissipation rates exists and the balance of these two processes varies. According to the time scales used here, the turbulence energy dissipation rate, denoting the viscous dissipation effects, is dominant over the scalar dissipation rate in an average sense, implying that the locations of intense reaction zones are strongly related to intense dissipation rate of turbulent kinetic energy for flame conditions investigated here.

For future work, similar DNS studies are needed under lean combustion conditions and high pressure conditions in a larger numerical domain. Also, chemical kinetics of hydrocarbon fuels as well as other alternative fuels need to be considered. The simple modelling approach proposed in this study may be applied for the filtered field.

Appendix A. Choice of progress variable

In the present study, non-unity Lewis numbers are considered. Naturally, it is considered that the choice of progress variable (i.e. temperature-based, Y_{H_2}-based) may affect the conclusions reported here, especially the result of the proposed unified model, due to differential diffusion contribution. Figure 15 shows scatter plots of $\tilde{c}_T$ and $\tilde{c}_{\mathrm{H}_2}$ colored based on the intensity of the mean reaction rate. Here c_{H_2} is the progress variable based on H_2 mass fraction. Particularly for mean reaction rate modelling, samples with large reaction rates are of interest which are denoted by dark-to-black colours in the plots. Clearly, the plots show that c_{H_2} tends to be larger than c_T in reaction zones for both cases and distribution is relatively broad, suggesting there is an influence of differential diffusion despite that most of reaction zones are located in intense turbulence regions ($Ka > 1$) as discussed in Figs. 11 and 12.

This results in a relatively large deviation from the DNS mean reaction rate and a large standard deviation when the individual flamelet (Eq. 23) and non-flamelet (Eq. 28) models are considered for c_{H_2} (see Figs. 16a, 16b, 16d and 16e) compared to the results for c_T. However, the unified approach proposed here in Eq. (29) tends to show a reduced deviation from the DNS mean reaction rate as well as its standard deviation compared to the individual model for c_{H_2} (Figs. 16c and 16f). Thus, the conclusion in the paper remains consistent regardless of the choice of a progress variable; both flamelet and non-flamelet models complement each others' weaknesses to predict a mean reaction rate, and performance of the unified approach proposed here tends to be less susceptible to the location on the regime diagram compared to the individual model considered. For more accurate mean reaction rate prediction for progress variables of lighter species using the proposed approach, the individual model and time scales considered in the unified model need to be improved.

Acknowledgments

This work is partially supported by Grant-in-Aid for Scientific Research (S) (No. 23226005) of Japan Society for the Promotion of Science (JSPS) and Cabinet Office/JSPS NEXT program (GR038).

References

[1] N. Swaminathan, G. Xu, A. P. Dowling, and R. Balachandran. Heat release rate correaltion and combustion noise in premixed flames. *J. Fluid Mech.*, 681:80–115, 2011.

[2] N. Swaminathan, R. Balachandran, G. Xu, and A. P. Dowling. On the correlation of heat release rate in turbulent premixed flames. *Proc. Combust. Inst.*, 33:1533–1541, 2011.

[3] Kyu Tae Kim and Dom A. Santavicca. Interference mechanisms of acoustic/convective disturbances in a swirl-stabilized lean-premixed combustor. *Combust. Flame*, 160:1441–1457, 2013.

[4] H.J. Krediet, C.H. Beck, W. Krebs, and J.B.W. Kok. Saturation mechanism of the heat release response of a premixed swirl flame using LES. *Proc. Combust. Inst.*, 34:1223–1230, 2013.

[5] J. Aminian, C. Galletti, S. Shahhosseini, and L. Tognotti. Key modeling issues in prediction of minor species in diluted-preheated combustion conditions. *Appl. Thermal Eng.*, 31:3287–3300, 2011.

[6] Y. Huang and V. Yang. Dynamics and stability of lean-premixed swirl-stabilized combustion. *Prog. Energy Combust. Sci.*, 35(4):293–364, 2009.

[7] M. Freitag and M. Klein. Direct numerical simulation of a recirculating, swirling flow. *Flow Turbul. Combust.*, 75:51–66, 2005.

[8] M. Day, S. Tachibana, J. Bell, M. Lijewski, V. Beckner, and R. K. Cheng. A combined computational and experimental characterization of lean premixed turbulent low swirl laboratory flames I. Methane flames. *Combust. Flame*, 159:275–290, 2012.

[9] M. Tanahashi, S. Inoue, M. Shimura, S. Taka, G-M Choi, and T. Miyauchi. Reconstructed 3D flame structures in noise–controlled swirl-stabilized combustor. *Exp Fluids*, 45:447–460, 2008.

[10] P Palies, D Durox, T Schuller, and S Candel. The combined dynamics of swirler and turbulent premixed swirling flames. *Combust. Flame*, 157:1698–1717, 2010.

[11] Evatt R. Hawkes, Ramanan Sankaran, and Jacqueline H. Chen. Estimates of the three-dimensional flame surface density and every term in its transport equation from two-dimensional measurements. *Proceedings of the Combustion Institute*, 33(1):1447–1454, 2011.

[12] N. Chakraborty, H. Kolla, R. Sankaran, E. R. Hawkes, J. H. Chen, and N. Swaminathan. Determination of three-dimensional quantities related to scalar dissipation rate and its transport from two-dimensional measurements direct numerical simulation based validation. *Proc. Combust. Inst.*, pages 1151–1162, 2013.

[13] S. Tanaka, M. Shimura, N. Fukushima, M. Tanahashi, and T. Miyauchi.

DNS of turbulent swirling premixed flame in a micro gas turbine combustor. *Proc. Combust. Inst.*, 33:3293–3300, 2011.

[14] V. Moureau, P. Domingo, and L. Vervisch. From Large-Eddy Simulation to Direct Numerical Simulation of a lean premixed swirl flame: filtered laminar flame-PDF modeling. *Combust. Flame*, 158:1340–1357, 2011.

[15] N. Swaminathan and K. N. C. Bray. Fundamentals and challenges. In *Turbulent premixed flames*, pages 1–40. Cambridge University Press, 2011.

[16] H. Wang, K. Luo, S. Lu, and J. Fan. Direct numerical simulation and analysis of a hydrogen/air swirling premixed flame in a micro combustor. *Int. J. Hydrogen Energy*, 36:13838–13849, 2011.

[17] E. Gutheil, G. Balakrishnan, and F. A. Williams. Structure and extinction of hydrogen–air diffusion flames. In N. Peters and B. Rogg, editors, *Lecture Notes in Physics: Reduced kinetic mechanisms for applications in combustion systems.*, pages 177–195. Springer Verlag, New York, 1993.

[18] R. J. Kee, G. Dixon-Lewis, J. Warnatz, M. E. Coltrin, and J. A. Miller. A Fortran computer code package for the evaluation of gas-phase multicomponent transport properties. *Sandia National Laboratories*, SAND86-8246, 1986.

[19] R. J. Kee, F. M. Rupley, and J. A. Miller. Chemkin-II: A Fortran chemical kinetics package for the analysis of gas phase chemical kinetics. *Sandia National Laboratories*, SAND89-8009B, 1989.

[20] N.B. Peter, D.B. George, and C. H. Alan. VODE, A Variable-Coefficient ODE solver. *SIAM J. Sci. Stat. Comput.*, 10:1038–1051, 1989.

[21] M. Tanahashi, M. Fujimura, and T. Miyauchi. Coherent fine-scale eddies in turbulent premixed flames. *Proc. Combust. Inst.*, 28:529–535, 2000.

[22] Y. Minamoto, N. Fukushima, M. Tanahashi, T. Miyauchi, T. D. Dunstan, and N. Swaminathan. Effect of flow-geometry on turbulence-scalar interaction in premixed flames. *Phys. Fluids*, 23(12):125107, 2011.

[23] M. Shimura, K. Yamawaki, N. Fukushima, Y. S. Shim, Y. Nada, M. Tanahashi, and T. Miyauchi. Flame and eddy structures in hydrogenair turbulent jet premixed flame. *Journal of Turbulence*, 13(42):1–17, 2010.

[24] B. Yenerdag, N. Fukushima, M. Shimura, M. Tanahashi, and T. Miyauchi. Turbulence-flame interaction and fractal characteristics of H_2-air premixed flame under pressure rising condition. *Proc. Combust. Inst.*, 35(2):1277–1285, 2015.

[25] T. Poinsot and S. Lele. Boundary conditions for direct simulations of compressible viscous flows. *J. Comput. Phys.*, 101:104–129, 1992.

[26] M. Baum, T. J. Poinsot, and D. Thévenin. Accurate boundary conditions for multicomponent reactive flows. *J. Comput. Phys.*, 116:247–261, 1994.

[27] Y. Wang, M. Tanahashi, and T. Miyauchi. Coherent fine scale eddies in turbulence transition of spatially–developing mixing layer. *Int. J. of Heat and Fluid Flow*, 28:1280–1290, 2007.

[28] N. Syred. A review of oscillation mechanisms and the role of the precessing vortex core (PVC) in swirl combustion systems. *Prog. Energy Combust. Sci.*, 32:93–161, 2006.

[29] O. Lucca-Negro and T. O'Doherty. Vortex breakdown: a review. *Prog. Energy Combust. Sci.*, 27:431–481, 2001.

[30] A.M. Steinberg, R. Sadanandan, C. Dem, P. Kutne, and W. Meier. Structure and stabilization of hydrogen jet flames in cross-flows. *Proc. Combust. Inst.*, 34(1):1499–1507, 2013.

[31] N. Peters. *Turbulent combustion.* Cambridge University Press, Cambridge, UK, 2000.

[32] K. N. C. Bray. The interaction between turbulence and combustion. *Proc. Combust. Inst.*, 17:223–233, 1979.

[33] R. Borghi and D. Dutoya. On the scales of the fluctuations in turbulent combustion. *Proc. Combust. Inst.*, 17(1):235–244, 1979.

[34] P. A. Libby and K. N. C. Bray. Implications of the laminar flamelet model in premixed turbulent combustion. *Combust. Flame*, 39(1):33–41, 1980.

[35] A. Mura and R. Borghi. Towards and extended scalar dissipation equation for turbulent premixed combustion. *Combust. Flame*, 133:193–196, 2003.

[36] N. Swaminathan and K. N. C. Bray. Effect of dilatation on scalar dis-

sipation in turbulent premixed flames. *Combust. Flame*, 143:549–565, 2005.

[37] H. Kolla, J. W. Rogerson, N. Chakraborty, and N. Swaminathan. Scalar dissipation rate modelling and its validation. *Comb. Sci. Technol.*, 181:518–535, 2009.

[38] N. Chakraborty and N. Swaminathan. Effects of Lewis number on scalar dissipation transport and its modeling in turbulent premixed combustion. *Comb. Sci. Technol.*, 182(9):1201–1240, 2010.

[39] T. D. Dunstan, Y. Minamoto, N. Chakraborty, and N. Swaminathan. Scalar dissipation rate modelling for Large Eddy Simulation of turbulent premixed flame. *Proc. Combust. Inst.*, 34:1193–1201, 2013.

[40] Y. Minamoto, T. D. Dunstan, N. Swaminathan, and R. S. Cant. DNS of EGR-type turbulent flame in MILD condition. *Proc. Combust. Inst.*, 34:3231–3238, 2013.

[41] D. B. Spalding. Mixing and chemical reaction in steady confined turbulent flames. *Proc. Combust. Inst.*, 13(1):649657, 1971.

[42] B. F. Magnussen and B. H. Hjertager. On mathematical modeling of turbulent combustion with special emphasis on soot formation and combustion. *Proc. Combust. Inst.*, 16:719–727, 1977.

[43] I. S. Ertesvåg and B. F. Magnussen. The eddy dissipation turbulence energy cascade model. *Comb. Sci. Technol.*, 159:213235, 2000.

[44] I. G. Gran and B. F. Magnussen. A numerical study of a bluff-body stabilized diffusion flame . Part 2. Influence of combustion modeling and finite-rate chemistry a numerical study of a bluff-body stabilized diffusion flame. *Comb. Sci. Technol.*, 119:191–217, 2007.

[45] Y. Minamoto and N. Swaminathan. Scalar gradient behaviour in MILD combustion. *Combust. Flame*, 161(4):1063–1075, 2014.

[46] Y. Minamoto, N. Swaminathan, R. S. Cant, and T. Leung. Reaction zones and their structure in mild combustion. *Comb. Sci. Technol.*, 186(8):1075–1096, 2014.

Table 1: Correlation coefficient for various fields. The coefficients are given for instantaneous and mean fields. The values in the brackets are those obtained using the samples taken from the combustion regions (progress variable bounded between 0.1 and 0.9).

Fields	ω_{c_T}- ϵ_{turb}	ω_{c_T}- ϵ_{c_T}	$\overline{\omega}_{c_T}$- $\widetilde{\epsilon}_{turb}$	$\overline{\omega}_{c_T}$- $\widetilde{\epsilon}_{c_T}$
S06	0.304 (0.34)	0.439 (0.37)	0.329 (0.36)	0.730 (0.73)
S12	0.510 (0.50)	0.435 (0.38)	0.903 (0.90)	0.653 (0.65)

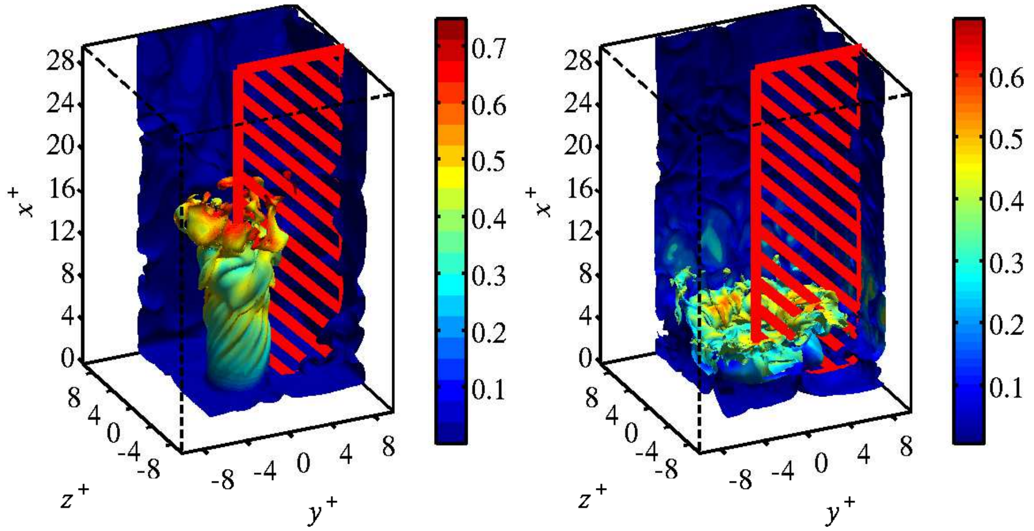

(a) (b)

Figure 1: Instantaneous 3D iso-surfaces of reaction progress variable $c_T = 0.5$ for (a) S06 and (b) S12 at $t = 11\tau_F$. Colour shows the normalised reaction rate $\omega^+_{c_T}$. Note that the iso-surfaces are not shown at $y^+ < -6$ and $z^+ < -6$ for visibility. The two-dimensional cross-section denoted by red lines shows the location of x-y plane considered in the following sections.

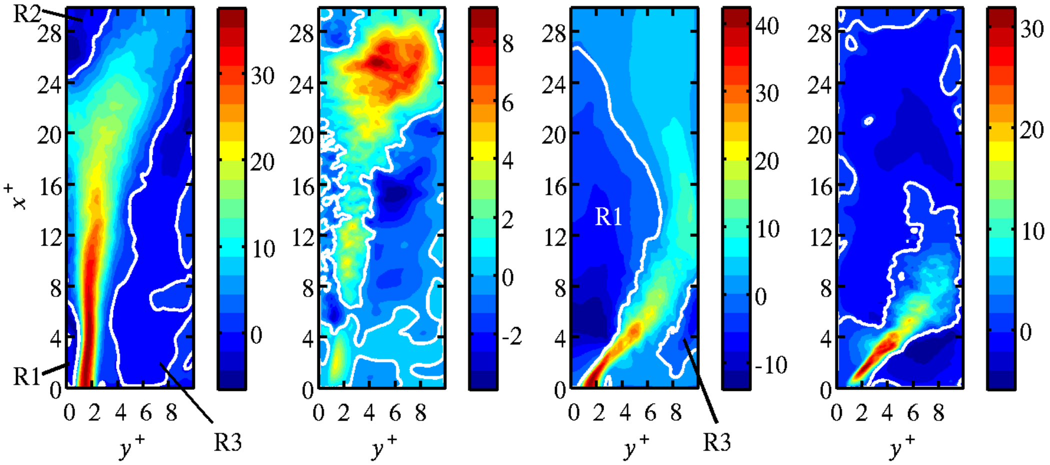

(a) (b) (c) (d)

Figure 2: Mean velocity component in the axial $\tilde{u}^+$ (a, c) and radial $\tilde{v}^+$ (b, d) directions for S06 (a, b) and S12 (c, d). The white contour line corresponds to $\tilde{u}^+ = 0$ and $\tilde{v}^+ = 0$.

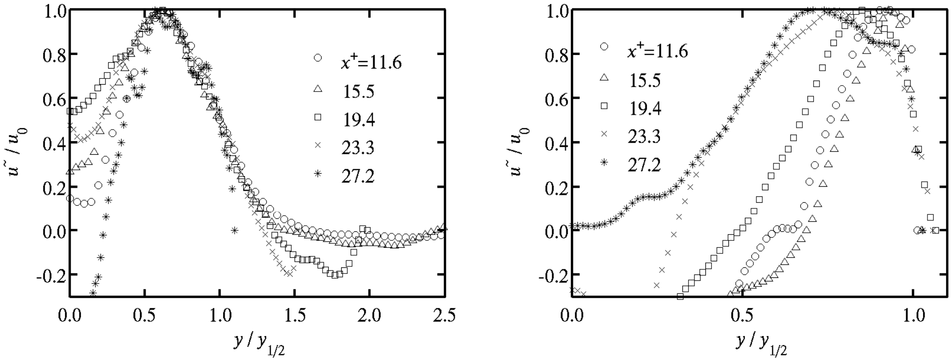

(a) (b)

Figure 3: Variation of $\tilde{u}/u_0$ with $y/y_{1/2}$ at x^+ =11.6, 15.5, 19.4, 23.3 and 27.2 for (a) S06 and (b) S12.

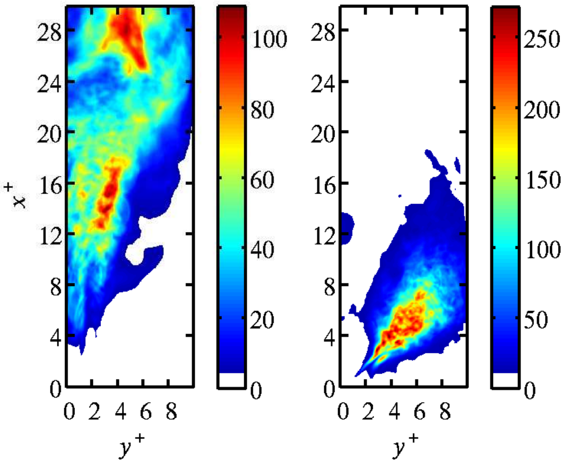

(a) (b)

Figure 4: Variation of normalised turbulent kinetic energy $\tilde{k}^+$ for (a) S06 and (b) S12.

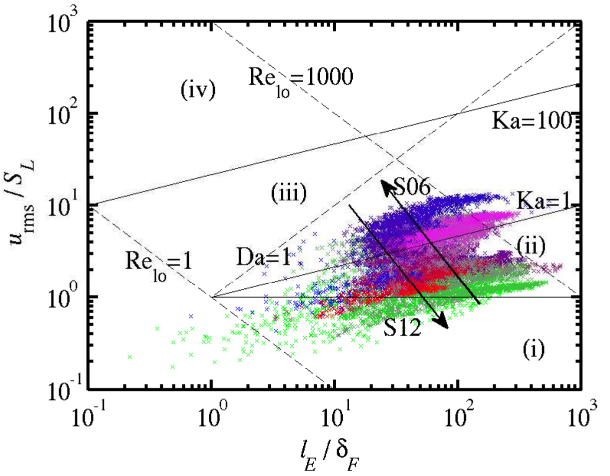

Figure 5: Local turbulent combustion conditions on the regime diagram for S06 and S12. The colour of data points depends on x^+ location of the samples. The colour changes from green to purple with an increase of x^+ distance of each sample for S06, and from blue to red for S12. The arrow denote general transition in the combustion regime with x^+ distance. One in every five samples is shown in the figure. (i) Wrinkled flamelets, (ii) Corrugated flamelets, (iii) Thin reaction zones and (iv) Broken reaction zones.

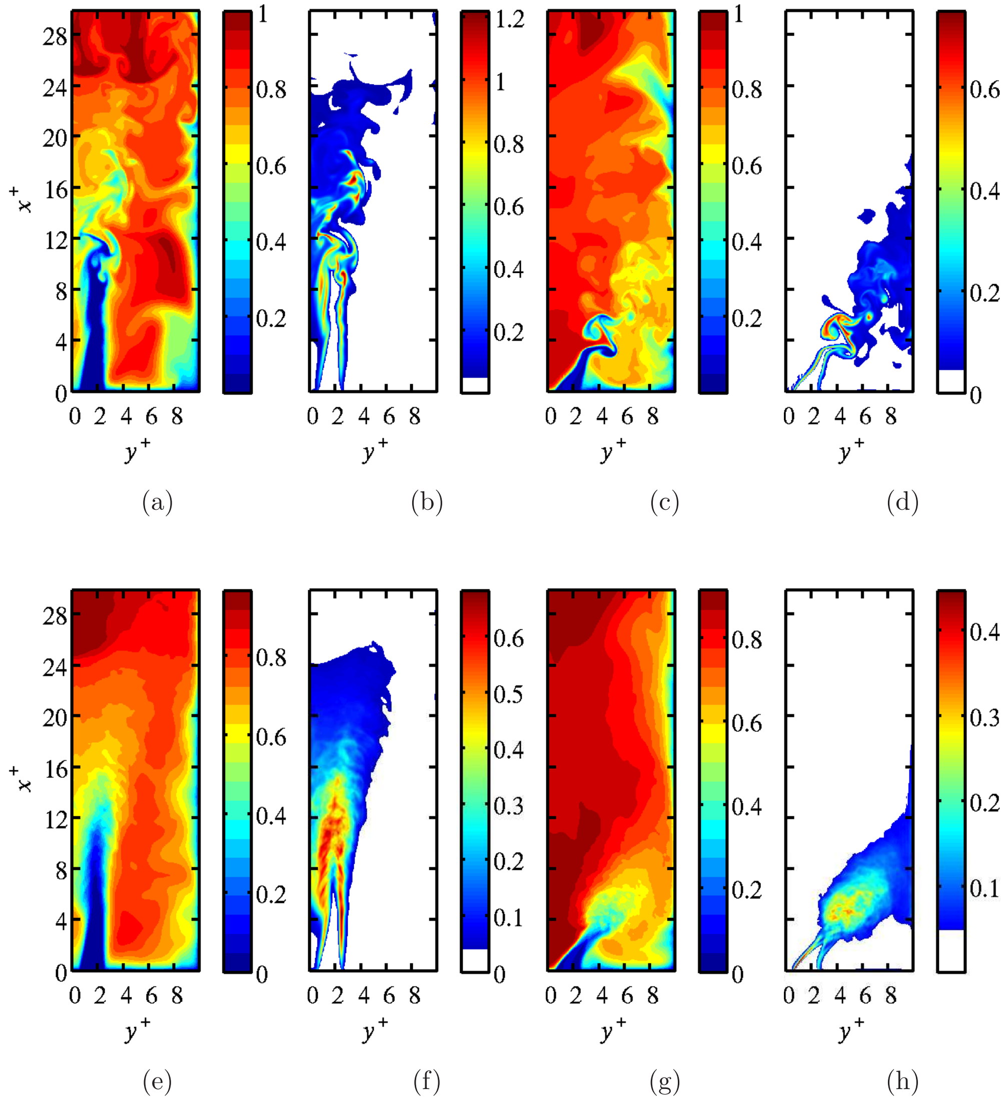

Figure 6: Variations of c_T (a, c), $\omega_{c_T}^+$ (b, d), $\tilde{c}_T$ (e, g) and $\bar{\omega}_{c_T}^+$ (f, h) for S06 (a, b, e, f) and S12 (c, d, g, h) in the 2D x-y plane marked in Fig. 1a.

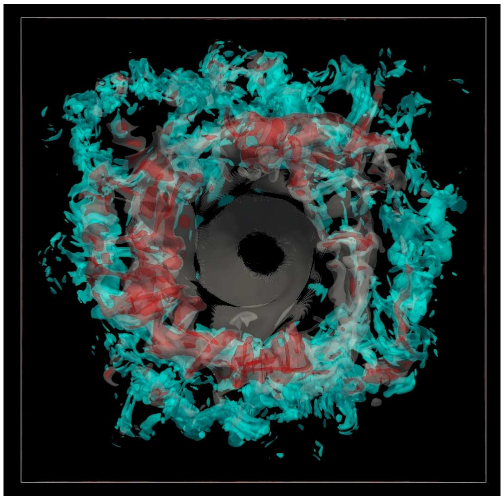

Figure 7: 3D instantaneous combustion field viewed from top to bottom in the x direction for S12. Cyan iso-surfaces: 10% of maximum ϵ_{turb}, white–grey iso-surfaces: $\omega^{+}_{c_T} = 0.5$ and red iso-surface: $\omega^{+}_{c_T} = 0.7$.

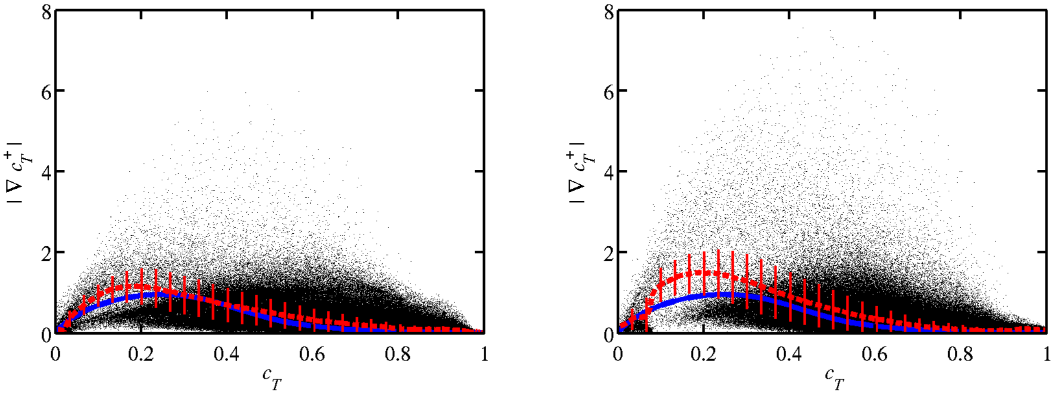

(a)

(b)

Figure 8: Scatter plot of instantaneous scalar gradient $|\nabla c_T|^+$ with the progress variable c_T, conditional average (red dashed line) and standard deviation (red thin line). The coresponding unstrained laminar flame solution is superimposed (blue line). The DNS samples are taken at $t = 11\tau_F$.

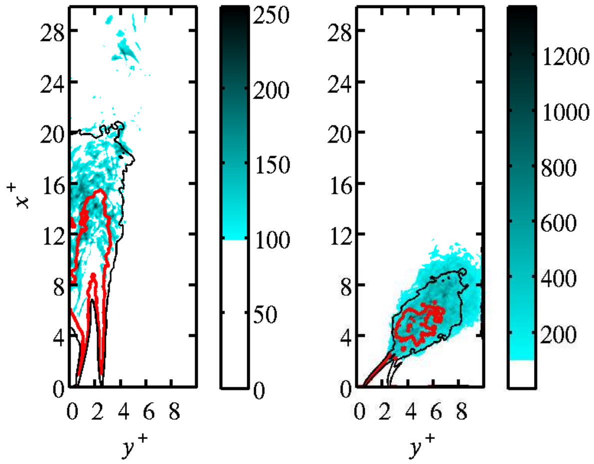

(a) (b)

Figure 9: Variation of normalised dissipation rate of turbulent kinetic energy $\tilde{\epsilon}^+_{turb}$ and reaction rate contours for (a) S06 and (b) S12. Thin black line: $\bar{\omega}^+_{c_T} = 0.1$ and bold red line: $\bar{\omega}^+_{c_T} = \omega^+_{1/2}$.

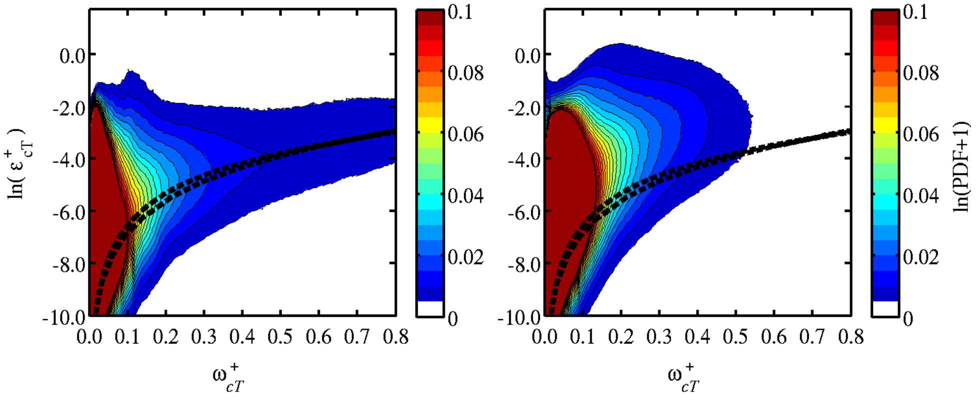

(a) (b)

Figure 10: Joint PDF of reaction rate and scalar dissipation rate, $P(\omega^+_{cT}, \ln \epsilon^+_{turb})$ for S06 (a) and S12 (b). For visibility, the colorbar is scaled as $0 \le \ln(\mathrm{PDF}+1) \le 0.1$. The maximum $\ln(\mathrm{PDF}+1)$ is 3.2 for S06 and 2.4 for S12. The contour lines are also superimposed for $0.005, 0.01, \cdots, 0.1$. Bold black line shows the corresponding unstrained laminar flame solution.

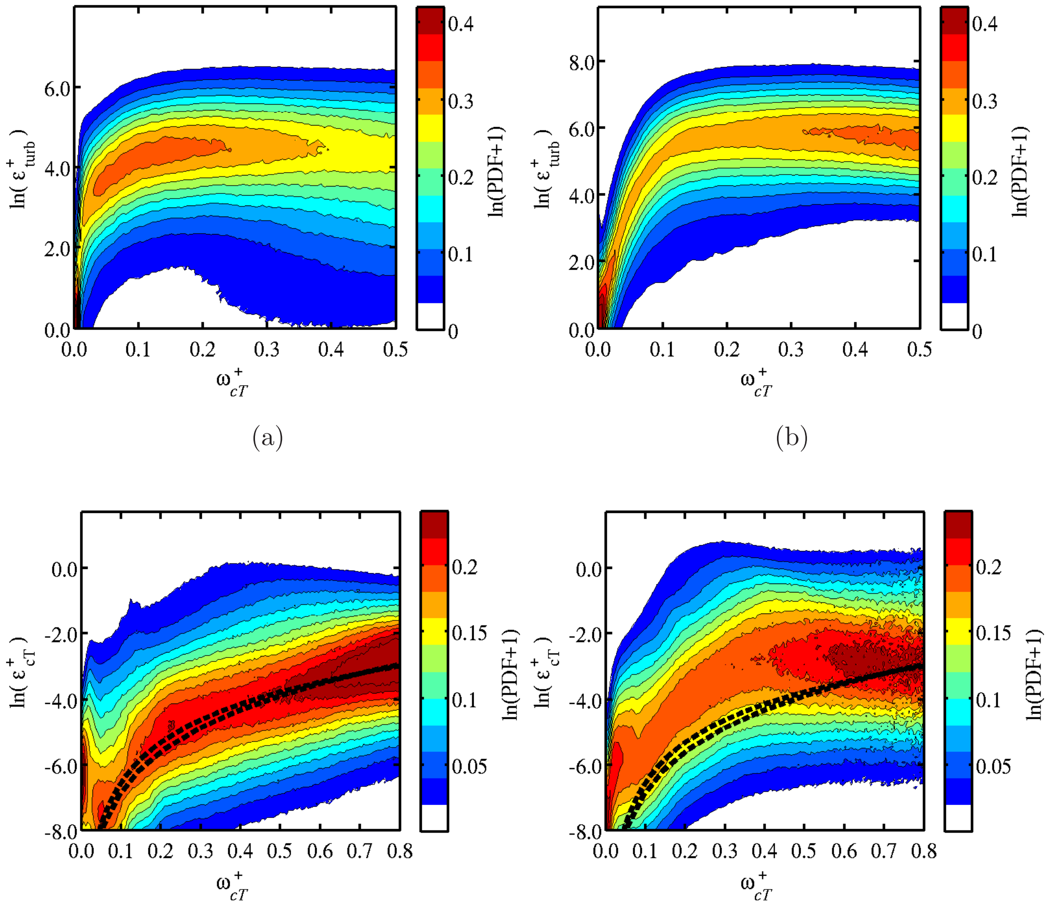

(a) (b)

(c) (d)

Figure 11: PDF of turbulence energy dissipation rate conditioned on reaction rate, $P(\ln \epsilon^{+}_{turb}|\omega^{+}_{c_T})$ (a, b) and PDF of scalar dissipation rate conditioned on reaction rate, $P(\ln \epsilon^{+}_{c_T}|\omega^{+}_{c_T})$ (c, d) for S06 (a, c) and S12 (b, d). The contour lines are also superimposed for $0.02, 0.04, \cdots, 0.24$ (a, b), and $0.035, 0.07, \cdots, 0.42$ (c, d). Bold black line shows the unstrained laminar flame solution (c, d).

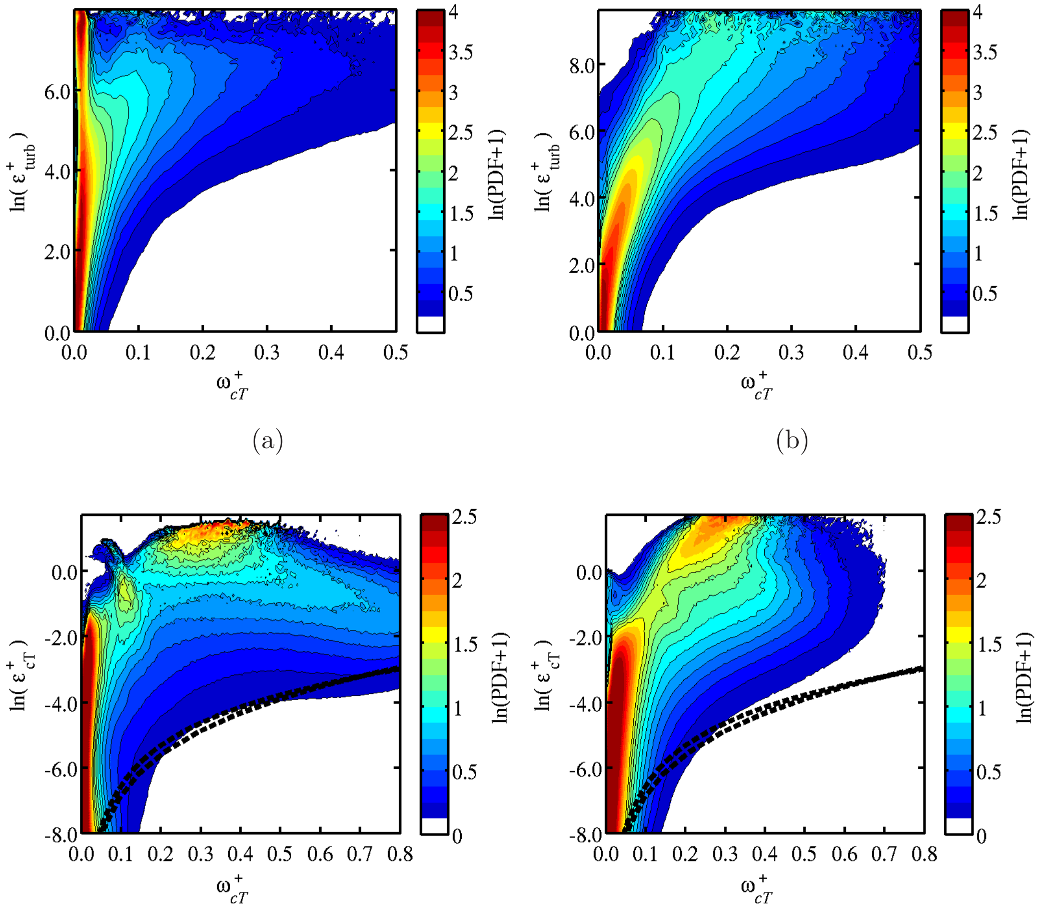

(a) (b)

(c) (d)

Figure 12: PDF of reaction rate conditioned on turbulence energy dissipation rate, $P(\omega_{c_T}^{+} | \ln \epsilon_{turb}^{+})$ (a, b) and PDF conditioned on scalar dissipation rate, $P(\omega_{c_T}^{+} | \ln \epsilon_{c_T}^{+})$ (c, d) for S06 (a, c) and S12 (b, d). The contour lines are also superimposed for $0.2, 0.4, \cdots, 2.0$ (a, b), and $0.125, 0.25, \cdots, 0.15$ (c, d). Bold black line shows the unstrained laminar flame solution (c, d).

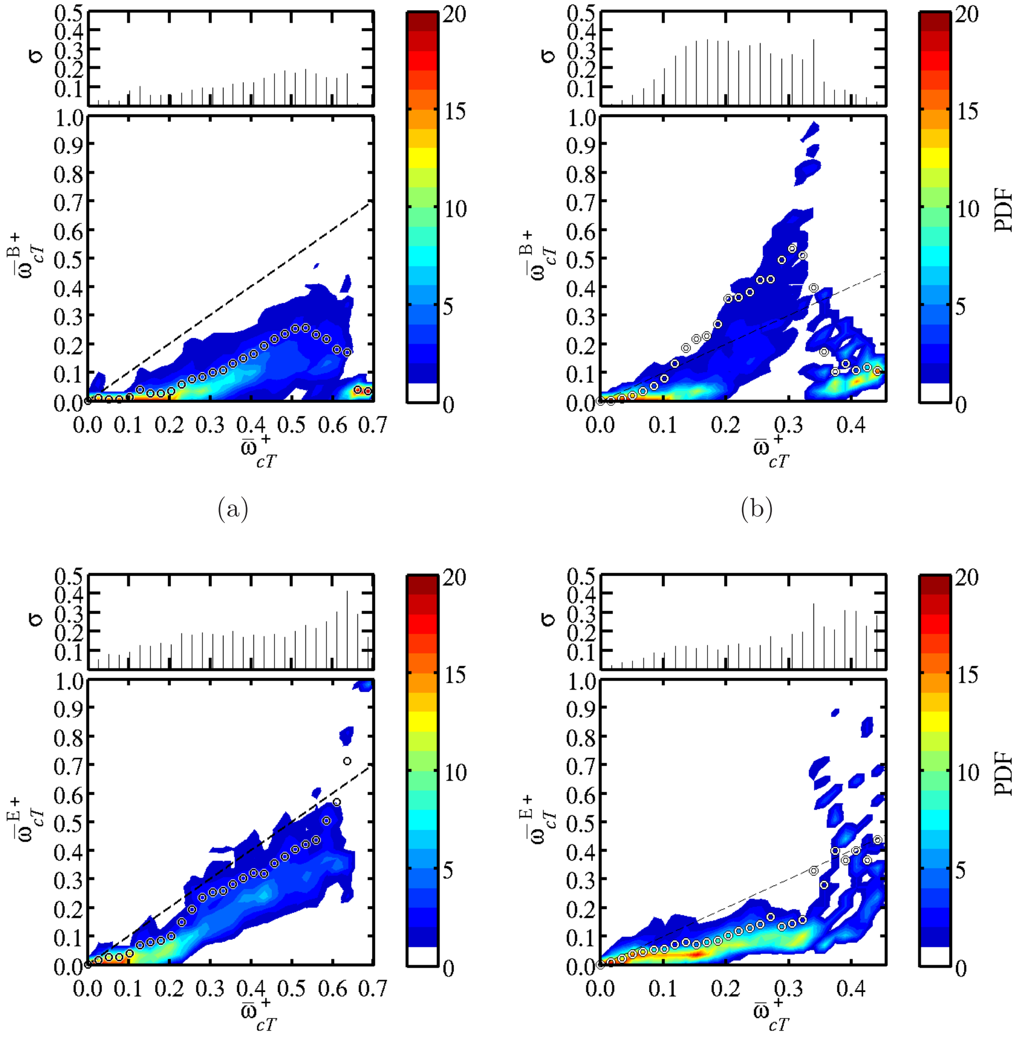

(a) (b)

(c) (d)

Figure 13: Conditional PDFs of reaction rate, $P(\bar{\omega}_{c_T}^{B\,+}|\bar{\omega}_{c_T}^{+})$ (a, b) and $P(\bar{\omega}_{c_T}^{E\,+}|\bar{\omega}_{c_T}^{+})$ (c, d) for S06 (a, c) and S12 (b, d). The mean reaction rates, $\bar{\omega}_{c_T}^{+}$, $\bar{\omega}_{c_T}^{B\,+}$ and $\bar{\omega}_{c_T}^{E\,+}$ are respectively reaction rates obtained directly from the DNS result, obtained using Eq. (23) and using EDC model (Eq. 28). The dashed line represents the perfect agreement. The white and black circles show conditional averages, $\langle\bar{\omega}_{c_T}^{B\,+}|\bar{\omega}_{c_T}^{+}\rangle$ (a, b) and $\langle\bar{\omega}_{c_T}^{E\,+}|\bar{\omega}_{c_T}^{+}\rangle$ (c, d), and one standard deviation σ from the average is shown in top of each figure.

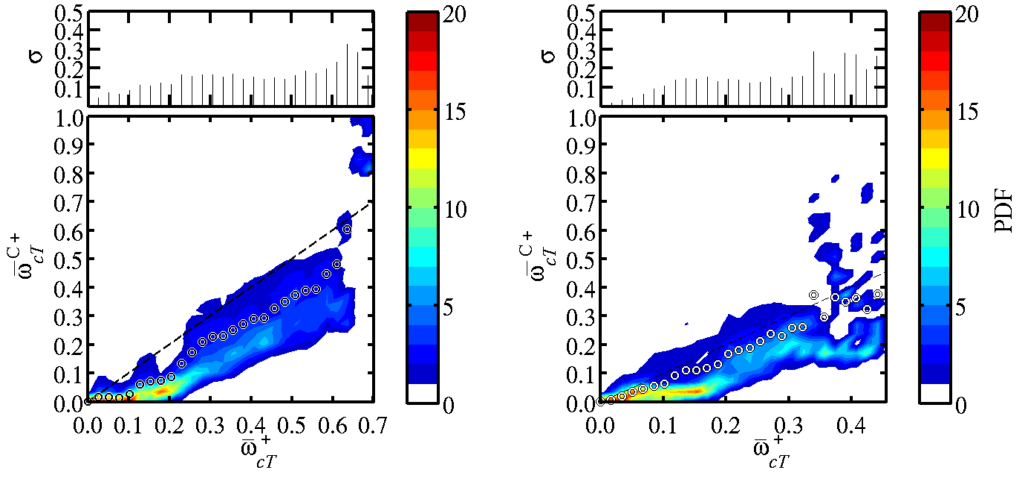

(a) (b)

Figure 14: Conditional PDF of reaction rate using Eq. (29), $P(\bar{\omega}_{c_T}^{C\ +}|\bar{\omega}_{c_T}^{+})$ for (a) S06 and (b) S12. The dashed line represents the perfect agreement. The white and black circles show conditional averages, $\langle\bar{\omega}_{c_T}^{C\ +}|\bar{\omega}_{c_T}^{+}\rangle$, and one standard deviation σ from the average is shown in the top of each figure.

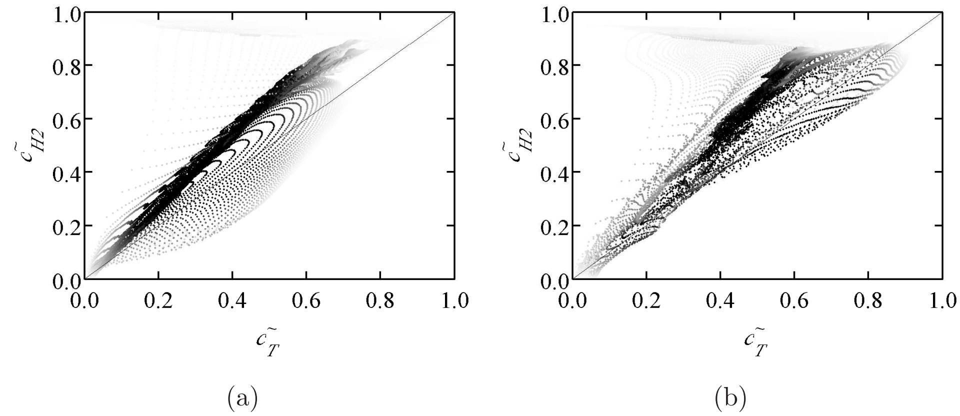

Figure 15: Scatter plot of $\tilde{c}_T$ and $\tilde{c}_{\mathrm{H}_2}$. Each scatter is coloured gradually from black to white based on the reaction rate $\bar{\omega}_{c_{\mathrm{H2}}}$. Black: high reaction rate, white: zero reaction rate. $\tilde{c}_T = \tilde{c}_{\mathrm{H}_2}$ boundary is denoted by solid line.

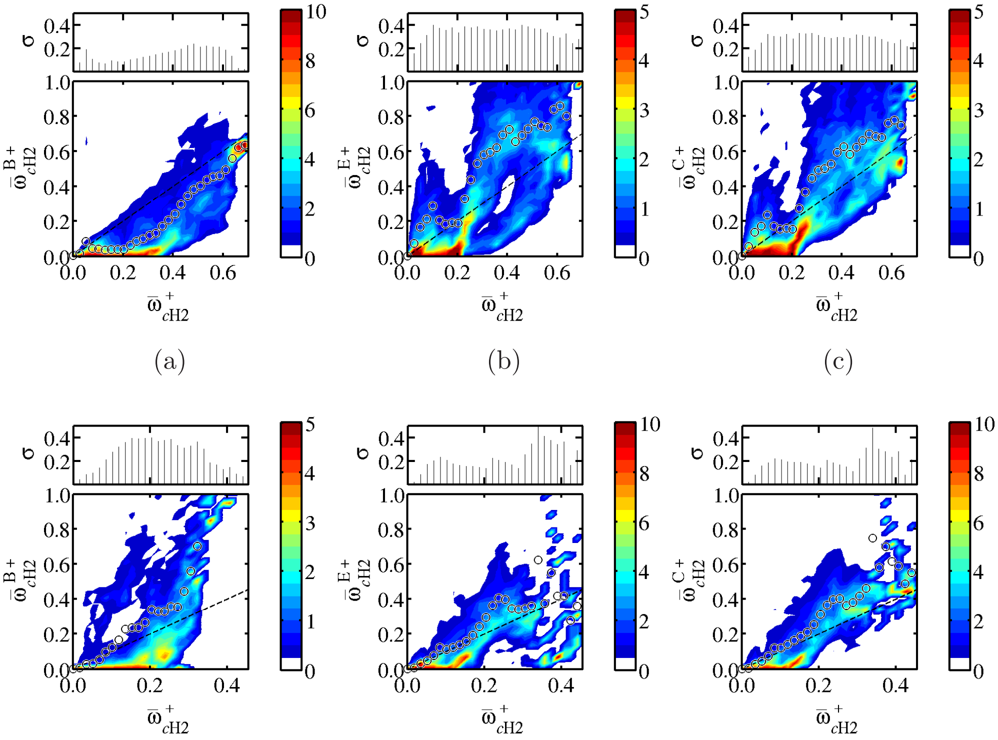

(a) (b) (c)

(d) (e) (f)

Figure 16: Conditional PDFs of reaction rate, $P(\bar{\omega}_{c_{\mathrm{H}_2}}^{B\,+}|\bar{\omega}_{c_{\mathrm{H}_2}}^{+})$ (a,d), $P(\bar{\omega}_{c_{\mathrm{H}_2}}^{E\,+}|\bar{\omega}_{c_{\mathrm{H}_2}}^{+})$ (b,e) and $P(\bar{\omega}_{c_{\mathrm{H}_2}}^{C\,+}|\bar{\omega}_{c_{\mathrm{H}_2}}^{+})$ (c,f) for S06 (a,b,c) and for S12 (d,e,f). The dashed line represents the perfect agreement. The white and black circles show conditional averages, $\langle\bar{\omega}_{c_{\mathrm{H}_2}}^{B\,+}|\bar{\omega}_{c_{\mathrm{H}_2}}^{+}\rangle$ (a,d), $\langle\bar{\omega}_{c_{\mathrm{H}_2}}^{E\,+}|\bar{\omega}_{c_{\mathrm{H}_2}}^{+}\rangle$ (b,e) and $\langle\bar{\omega}_{c_{\mathrm{H}_2}}^{C\,+}|\bar{\omega}_{c_{\mathrm{H}_2}}^{+}\rangle$ (c,f), and one standard deviation σ from the average is shown in top of each figure.